Journal of Materials Chemistry A

ROYAL SOCIETY OF CHEMISTRY

PAPER

View Article Online
View Journal | View Issue

Cite this: J. Mater. Chem. A, 2023, 11, 15286

The role of phonons in switchable MOFs: a model material perspective†

Alexander E. J. Hoffman, ‡[a] Irena Senkovska, ‡*[b] Leila Abylgazina,[b] Volodymyr Bon, [b] Veronika Grzimek,[c] Anna Maria Dominic,[d] Margarita Russina, [c] Marvin A. Kraft,[e] Inez Weidinger, [e] Wolfgang G. Zeier, [e] Veronique Van Speybroeck *[a] and Stefan Kaskel*[b]

The large cell volume changes of switchable metal–organic frameworks (MOFs) render them as promising functional materials. Low-frequency phonon modes are known to influence the dynamic response of these materials. The pillared layer DUT-8(M) materials are prototypical examples of switchable MOFs, enabling switching between the closed and open pore phases, largely depending on the metal ions constituting the paddle wheel unit. However, the role of specific phonon modes in the softness of these materials is still rather unexplored. This study combines complementary spectroscopic techniques such as Raman spectroscopy, inelastic neutron scattering, and phonon acoustic spectroscopy (PAS) with density functional theory calculations (DFT) to unravel the vibrational properties of DUT-8(M) with different metal nodes (M = Ni, Co, Zn, Cu) to address these open questions. After analysis of the various experimental and theoretical spectroscopic data, the closed pore phase of DUT-8(Ni) appeared to be stiffer than that of the materials with Co and Zn. Experiments also show that the open pore phase of the Ni based compound is softer than those containing Zn and Co, although these findings could not be supported by theory. Nevertheless, DFT calculations could explain that changing the metal atom has mainly an impact on the phonon modes inducing changes in the paddle wheel unit. These results yield valuable insights into the role of the metal node on the observed flexibility in DUT-8(M) materials and can help to understand the mechanisms behind the phase transition in switchable MOFs.

Received 12th April 2023
Accepted 23rd June 2023

DOI: 10.1039/d3ta02214e

rsc.li/materials-a

1 Introduction

Switchable metal–organic frameworks (MOFs), offering unique structural transformations and pore opening accompanied by large cell volume changes in response to external stimuli,[1–3] are promising materials for sensing,[4] separations,[5] catalysis,[6] and drug delivery.[7–9] The dynamics of these materials can be induced by the removal/incorporation of guest molecules,[10] pressure, photo- and thermostimulation.[11–15] Stimuli-responsive behaviour is accompanied by structural changes, which lead not only to a variation in porosity but also in characteristic vibrational fingerprints.[16–19] A thorough vibrational analysis provides important insight into elastic moduli, reflecting the softness/stiffness of switchable MOFs (compliance). Furthermore, it remains an open question if certain phonons (soft modes) can be identified as initiating the inelastic transition.

Both experimental and computational approaches are intensively used to quantify mechanical properties of switchable MOFs such as bulk modulus, directional and hardness Young's modulus, shear modulus, and Poisson's ratio.[20,21] Among experimental techniques, high-pressure crystallography,[22,23] nano-indentation,[24] atomic force microscopy,[25] Brillouin scattering experiments[26] can be named. Single-crystal nano-indentation experiments revealed the dynamic mechanical behaviour of $[Zn_2(L)_2(dabco)]_n$ (L = linear dicarboxylate linker, dabco = 1,4-diazabicyclo[2.2.2]octane) in various solvents (*e.g.* from ~2.08 GPa with *N*,*N*-dimethylformamide (DMF) to ~6.53 GPa with toluene on the 001 facets), attributed to guest-induced changes to the network geometry.[24] High-pressure diffraction data revealed swelling behaviour of ZIF-8

[a]Center for Molecular Modeling, Ghent University, Technologiepark 903, 9052 Zwijnaarde, Belgium. E-mail: Veronique.VanSpeybroeck@UGent.be
[b]Chair of Inorganic Chemistry I, Technische Universität Dresden, Bergstr. 66, 01069 Dresden, Germany. E-mail: Irena.Senkovska@tu-dresden.de; Stefan.Kaskel@tu-dresden.de
[c]Helmholtz-Zentrum Berlin für Materialien und Energie, Lise-Meitner-Campus, Hahn-Meitner-Platz 1, 14109 Berlin, Germany
[d]Chair of Electrochemistry, Technische Universität Dresden, Zellescher Weg 19, 01062, Dresden, Germany
[e]Institute of Inorganic and Analytical Chemistry, Westfälische-Wilhelms-Universität Münster, Correnstr. 30, 48149 Münster, Germany

† Electronic supplementary information (ESI) available: PXRD patterns, adsorption isotherms, SEM images, optimized structural parameters from static DFT calculations visualization of experimental and theoretically optimized crystal structures, mode character for terahertz vibrations, theoretical structures with disintegrated paddle wheel unit. See DOI: https://doi.org/10.1039/d3ta02214e

‡ Contributed equally.

instead of compression upon pressure increase to 0.18 GPa, which is now known as "hyperfilling" of the MOF pores with hydrostatic fluids.[27] Computational investigations of ZIF-8 mechanical properties revealed shear-mode softening behaviour, since elastic constants (shear modulus) decrease with increasing pressure from 0 to 0.35 GPa.[28] In order to obtain information related to a crystalline material's elasticity (elastic constant tensor), Coudert and co-workers determined the mechanical properties of MIL-53(Al) and several other wine-rack type MILs through DFT calculations, demonstrating significant anisotropy in the Young's modulus which they attribute to the flexibility of the framework in two dimensions.[29]

The combination of experiments and theory has also proven to be helpful in understanding the lattice dynamics in flexible MOFs. For example, the pioneering work of Ryder *et al.*[30] applied inelastic neutron scattering (INS) experiments and infrared (IR) spectroscopy supported by density functional theory (DFT) calculations to investigate the terahertz vibrations in ZIFs, including the gate-opening mode in ZIF-8. This shows that the theoretical prediction of experimental terahertz spectra is crucial to identify the soft phonon modes in MOFs.[16,31] A similar experimental/theoretical approach was reported for MIL-53(Al),[32] through IR and Raman spectra, characteristic vibrations were identified, which may influence the breathing mechanism. The theoretical calculations demonstrated also that linker substitutions in flexible MIL-53 analogues have a large effect on the rigid-unit mode frequencies, whereas this is less so for inorganic chain substitutions.[17]

In our efforts to achieve a better understanding of node and hinge dynamics leading to adsorption-induced flexibility, we report here insights into elastic characteristics and associated intrinsic framework softness for a model system DUT-8(M), which can be synthesized with a variety of metal nodes containing Ni, Co, Zn, or Cu.[33] We are particularly interested in the influence of the metal on the vibrational dynamics and soft modes alterations inducing the deformation of the lattice.

DUT-8 with a composition of $[M_2(2,6\text{-ndc})_2\text{dabco}]_n$ (2,6-ndc – 2,6-naphthalene dicarboxylate) is a well-studied representative of the pillared layer MOF family, containing the dinuclear paddle wheel unit ($M_2(COO)_4$) acting as nodes and naphthalene as linker core (see Fig. 1).[33,34] The compounds show pronounced flexibility upon desolvation (formation of the closed pore (cp) phase) and adsorption of fluids (reopening to the open pore (op) phase).[35] The dynamic response of the frameworks in this series of gate opening MOFs is strongly dependent on chemical composition (metal in the node),[36,37] but also the particle size has a decisive influence on the structural switching behaviour between an op and a cp states.[38–40] Thus, the flexibility is determined by *e.g.* the stiffness of the node, the dispersive interactions between the linkers, and/or the surface energy and may affect the adsorption properties.[37,41] Moreover, it was demonstrated that the solvent in the network's pores governs the framework's structural features in the solvated state.[42,43]

DUT-8 frameworks show remarkable selectivity in CO_2/CH_4, $CH_2Cl_2/CHCl_3/CH_3Cl$ as well as D_2/H_2 separation which can be tailored by metal substitution.[36,41,44,45] In seeking to establish a better understanding of the role of lattice vibrations impacted by the bonding strength of various metals (*i.e.* Ni, Co, Zn, and Cu), in the following, we combine complementary experimental techniques, in particular Raman spectroscopy, inelastic neutron scattering, and phonon acoustic spectroscopy, to unravel the impact of phonon frequencies on flexibility. The interpretation of these experiments is corroborated by theoretical calculations yielding insight in the low-frequency phonon modes governing the flexibility.

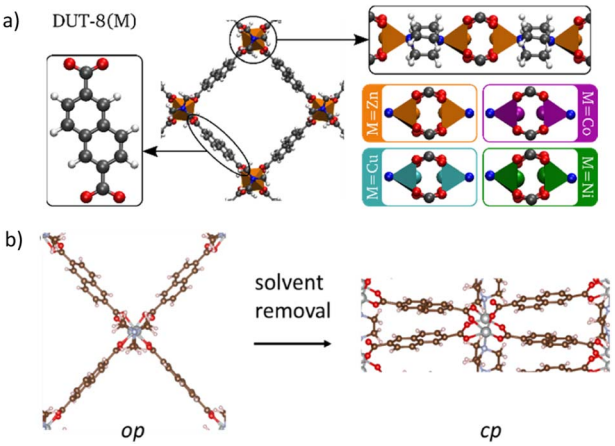

Fig. 1 (a) Visualization of the op phase of DUT-8(M) with the 2,6-ndc linker, the dabco pillar and the dinuclear paddle wheel unit (M = Zn, Co, Cu, or Ni); (b) visualization of the structural transition in DUT-8(M) from the open pore (op) to the closed pore form (cp) for M = Ni.

2 Results and discussion

2.1 Synthesis and basic characterization of DUT-8(M), M = Ni, Co, Zn, Cu

The DUT-8(M) samples, based on Ni, Co, and Zn were synthesized as macro-sized or submicron-sized crystals (for more details see Experimental Part and ESI, Section 1†).[33,38,40,41] In contrast to switchable macro-sized crystals transforming to the cp phase upon desolvation, the submicron-sized particles allow to perform the measurements on desolvated, solvent-free op materials, since they do not transform to the cp phase after desolvation (Fig. S1a†).

Powder X-ray diffraction (PXRD) patterns for all as-synthesized compounds are in good agreement with the patterns calculated from the single crystal structures (Fig. S1b, S4a and S7a†), indicating that all samples are phase pure and isomorphous.

The desolvation of the macro-sized Ni, Co, and Zn based compounds leads to the cp phases (Fig. 1b), as confirmed by PXRD patterns (Fig. S1c and S4b†). The porosity of the desolvated materials was verified by nitrogen physisorption (Fig. S2a and b†).

The macro-sized particles of DUT-8(Cu) mainly remain in the op phase after solvent removal (Fig. S1a†) or collapse to the new interpenetrated, confined closed pore (ccp) phase, structurally differing from the cp phase known for Ni, Co and Zn based compounds.[46] The ccp phase of DUT-8(Cu) was not investigated further in this work.

The desolvation of the submicron-sized particles of DUT-8(M) containing Co and Ni as expected led to the solvent free op phases, according to the PXRD analysis (Fig. S1a†).

2.2 Crystal structures of investigated compounds

2.2.1 Open pore phases. The solvated samples of DUT-8 based on Ni, Co, Zn, and Cu show only minor differences in the crystal structures (see Table S2 and Fig. S8–S11†). Comparing the experimental structural parameters of the structures crystallizing in the *C*2/*m* space group shows slight variations in the cell volumes between 3125 and 3303 Å^3. The longest M⋯M distance in the paddle wheel is found for the Zn based compound, while in the Ni, Co, and Cu based MOFs, the M⋯M spacing is comparable. Furthermore, the Cu based MOF stands out with the largest bond length between the metal and the nitrogen atom of the dabco ligand. The N–M bond for the Co compound is shorter but still slightly longer than for Ni and Zn. This is comparable to the Jahn–Teller elongation in sixfold coordinated M(II) (M = Co, Cu) complexes.[47] According to the magnetic measurements, the Co in DUT-8(Co) is supposed to be present in the high spin state,[41] known to induce a weak Jahn–Teller effect, in contrast to Cu, which is prone to strong Jahn–Teller distortion in the presence of certain ligands.

The structural parameters of the theoretically optimized op structures largely show the same trends as those in the experimental structures, except for the M⋯M distance and the M–N bond length in DUT-8(Co) (see Table S2 and Fig. S8–S11†).

2.2.2 Closed pore phases. After desolvation, the resulting solvent-free phases show more significant differences in the experimental crystal structures (Table S3 and Fig. S12–S14†). In the cp phases, the 2,6-ndc linkers are closely packed and tend to optimize their alignment to maximize the dispersion interactions of the linker core at the expense of a distorted coordination geometry of the metals.

In the case of DUT-8(Ni)_cp, the adjacent O–Ni–O angles are ranging between 61° and 110°, pointing on very strong distortion from the square-pyramidal coordination geometry (Fig. 2 and S12†). Thus, the bending of the carboxylate hinges is expected to be the main origin of the "gate opening" mechanism. In contrast, the coordination geometry of the Co cluster within DUT-8(Co)_cp undergoes only minor changes during the closing (Fig. 2 and S13†). The corresponding O–Co–O angles are between 91° and 97°, but the $Co_2(COO)_4$ unit shows strong shear deformation, altering the angle between the N⋯N (dabco) and M⋯M (paddle wheel) axes significantly. The corresponding M–M–N angle in DUT-8(Ni)_cp structure is 153.9°, whereas in DUT-8(Co)_cp it amounts to 141.5°.[41]

In DUT-8(Zn), the M⋯M distance is the longest among all members of DUT-8(M)_cp series (3.80 Å, Table S3†), which leads to a strong elongation of some Zn–O bonds (Fig. 2 and S14†). Hence, the paddle wheel unit disintegrates and the coordination polyhedron changes from quadratic pyramidal to distorted tetrahedral. The disintegration of the paddle wheel unit by detachment of two Zn–O bonds yields more freedom to the 2,6-ndc linkers to acquire a favourable stacking driven by dispersion interactions.[38,48] The experimental properties of the DUT-8(Cu)_cp phase cannot be discussed in the present work, since this phase was not observed experimentally.

The theoretically optimized structure of DUT-8(Ni)_cp has structural parameters which are very close to the experiment. The predicted structural parameters of the materials with other metal compounds are similar to those of DUT-8(Ni)_cp and, hence, deviate from the experimentally obtained values (see Table S3 and Fig. S12–S14†). For the Zn compound, this can largely be explained by the disintegrated paddle wheel unit in the experimental structure.

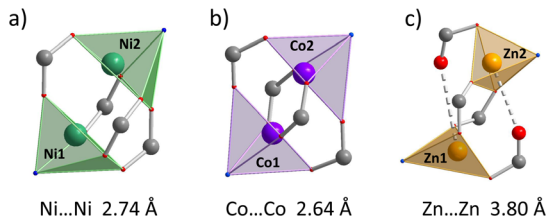

Fig. 2 Paddle wheel unit in the closed pore phases of DUT-8(Ni) (a), DUT-8(Co) (b), DUT-8(Zn) (c).

2.3 Calculation of terahertz vibrations

To gain initial insight into the low-frequency vibrational spectrum of the different DUT-8(M) (M = Ni, Co, Zn, Cu) compounds, their lattice vibrations in the gamma point were predicted for both the op and cp phases. The analysis is restricted to the 30 eigenmodes with the lowest frequencies, as these will mainly govern the flexible behaviour. The modes are described by subdividing them in translations and rotations of the separate building blocks (see Section 2.3.1). The normal modes of the Ni^{2+}, Co^{2+} and Cu^{2+} compounds will be discussed in comparison to the Zn compound since the influences of the spin state can be neglected for Zn^{2+}, and it may serve as a nonmagnetic reference for the isostructural compounds containing 3d transition metals.[49] As the experimental cp phase structure of DUT-8(Zn) exhibits a disintegrated paddle wheel unit, the impact of this disintegration on the terahertz modes will also be discussed here.

2.3.1 Open pore phases. In the op phases we, as expected, identified three translational modes with (almost) zero frequency (see Fig. 4). Noteworthy frequency differences occur for the Raman inactive modes involving rotations of the dabco linker (modes A in Fig. 4, 3b and S15†): DUT-8(Co) has frequencies comparable to DUT-8(Zn), whereas the frequencies within DUT-8(Cu) have become imaginary and those of DUT-8(Ni) are considerably higher. The near-zero frequency in the Zn, Co and Cu compounds indicates that the dabco rotation is almost unhindered. In contrast, the frequency of this mode within DUT-8(Ni) is higher due to a slight distortion of the paddle wheel unit, which possibly hinders the dabco rotation.

Next, we find a mode with a very low frequency, around 15 cm^{-1} in DUT-8(Zn) that has a significantly higher frequency in the other three structures (mode B in Fig. 4). This mode can be described by translations of the paddle wheel and dabco units combined with a rotational motion of the 2,6-ndc linkers

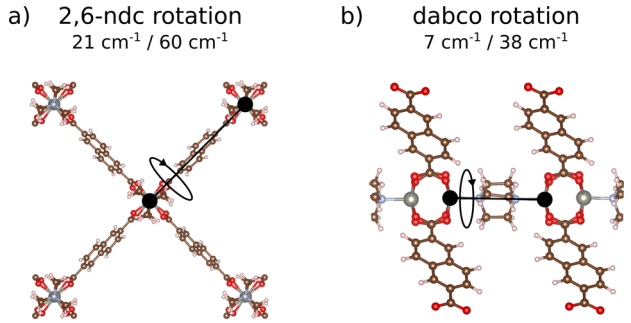

Fig. 3 Schematic visualization of the normal modes involving rotations of the 2,6-ndc linker (Raman active) (a) and dabco linker (Raman inactive) (b) in the op phase of DUT-8(Zn). Static DFT predictions of the normal mode frequencies are presented for the op/cp phase of DUT-8(Zn).

(see Fig. S16†). The frequency of this mode in DUT-8(Zn) is lower, probably because the 2,6-ndc linker is already tilted, facilitating the translation of the other building blocks.

Furthermore, we observe several normal modes that display frequency differences of (less than) 5 cm^{-1} between the different structures, showing that the choice of the metal atom has no impact on them (modes C). They involve mainly rotations (see Fig. 3a and S17†) and translation (see Fig. S18†) of the 2,6-ndc linker.

At even higher frequencies, several terahertz modes exhibit subtle frequency differences but no clear trend appears. Consequently, and given their relatively high frequency, it is not expected that they have a large influence on the flexibility. Except for two modes around 75 cm^{-1} exhibiting mainly internal vibrations, which show very large frequency differences between the structures (modes D in Fig. 4). They involve a distortion of the dabco unit due to the rotation of the two NC_3H_6 units in the opposite direction (see Fig. S19†). They have a much lower frequency in DUT-8(Cu), probably because these dabco units are less distorted compared to DUT-8(Zn). In contrast, the vibrational frequencies of these modes in DUT-8(Ni) are much higher, which may be linked to an increased distortion of the dabco unit.

Finally, above 75 cm^{-1} a single mode yields frequency differences larger than 20 cm^{-1} (mode E). This is because this mode has a different mode character in DUT-8(Zn) and DUT-8(Cu) on the one hand (mix of dabco translations and linker rotations) and in DUT-8(Co) and DUT-8(Ni) on the other hand (mainly linker rotations) (see also Fig. S29†). This different mode character could originate from a decreased length of the 1D chain formed by the paddle wheel and dabco units in the latter compounds.

In summary, differences in the paddle wheel unit mainly cause the frequency differences: the Ni based paddle wheel unit is more distorted than the one with Zn, which, in its turn, is more distorted than the Cu paddle wheel unit. Thus, the presence of Ni increases the vibrational frequency of several terahertz modes, which may stiffen the op phase of DUT-8(Ni) compared to Zn whereas the opposite is true when Cu is used as the metal atom. The terahertz frequencies of DUT-8(Co) are similar to those of DUT-8(Zn). For the Ni, Zn, and Co based compound this finding are in agreement with the experimental observations. The stabilisation of the metastable open pore phase is possible in much larger crystals for DUT-8(Ni) than it is the case for DUT-8(Zn) and DUT-8(Co).[38,40,41]

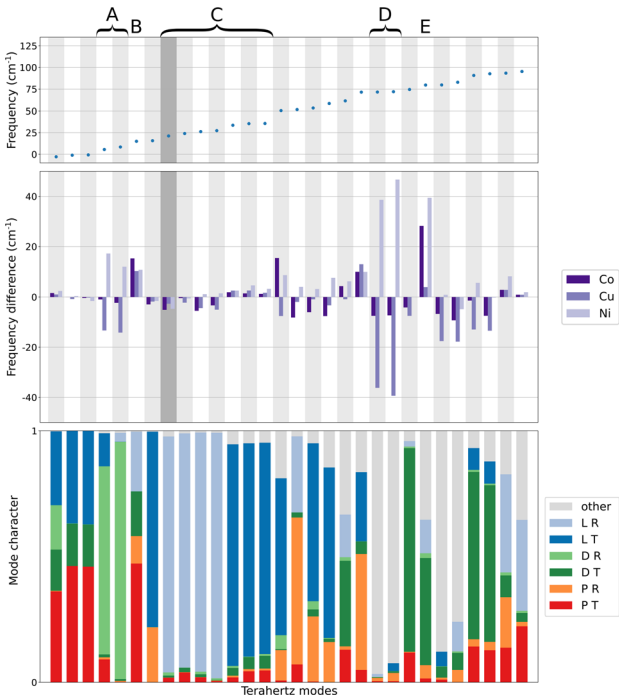

Fig. 4 Characterization of the 30 normal modes with the lowest frequencies of DUT-8 materials in their op phase. Top: Vibrational frequencies of the different terahertz vibrations within DUT-8(Zn). Middle: Frequency difference between corresponding modes of DUT-8(Co), DUT-8(Cu), or DUT-8(Ni) and DUT-8(Zn). Bottom: Subdivision of the displacements within each terahertz mode of DUT-8(Zn) in translations (T) and rotations (R) of the 2,6-ndc linker (L), the dabco linker (D), the paddle wheel unit (P), and other types of motions. The normal modes discussed in Section 2.3.1 are labelled at the top of the figure. The Raman active normal mode involving rotations of the 2,6-ndc linker is highlighted in dark grey.

2.3.2 Closed pore phase. For the cp phase structures, we observe only small frequency differences for terahertz vibrations below 50 cm^{-1} (see Fig. 5). In that range, we again find the translation modes with a frequency of 0 cm^{-1}. The next three modes with the lowest vibrational frequency (modes B in Fig. 5) combine either translations of the paddle wheel unit and the dabco linker with rotations of the 2,6-ndc linker (see Fig. S20 and S21†) or translations of the 2,6-ndc linker with rotations of the paddle wheel unit (see Fig. S22†).

These modes have a slightly reduced frequency in the three structures other than DUT-8(Zn) potentially softening these materials. In contrast to the op phase structures, the modes involving dabco rotations (modes A in Fig. 5) have a non-negligible frequency as this rotation is hindered in the denser cp phase (see Fig. S23†). As a result, the distortion of the paddle wheel unit has less effect on the vibrational frequency yielding almost equal values for all four structures.

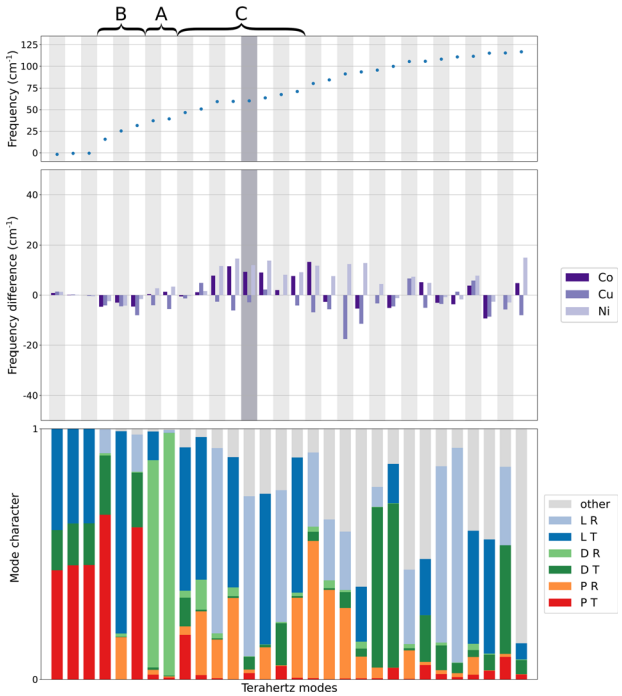

Fig. 5 Characterization of the 30 normal modes with the lowest frequencies of DUT-8 materials in their cp phase. Top: Vibrational frequencies of the different terahertz vibrations within DUT-8(Zn). Middle: Frequency difference between corresponding modes of DUT-8(Co), DUT-8(Cu), or DUT-8(Ni) and DUT-8(Zn). Bottom: Subdivision of the displacements within each terahertz mode of DUT-8(Zn) in translations (T) and rotations (R) of the 2,6-ndc linker (L), the dabco linker (D), the paddle wheel unit (P), and other types of motions. The normal modes discussed in Section 2.3.2 are labelled at the top of the figure. The Raman active normal mode involving rotations of the 2,6-ndc linker is highlighted in dark grey.

Also the vibrations, inducing rotations and translations of the 2,6-ndc linker, have an increased vibrational frequency compared to the op phase (modes C) due to the increased hindrance of these modes. For translations of opposite linkers in the same direction, the choice of metal atoms does not affect the vibrational frequency of these modes (see Fig. S24 and S25†). For all the other modes involving translations or rotations of the 2,6-ndc linker (see Fig. S26–S28†), the choice for Co or Ni metal atoms increases the vibrational frequency of these modes. Therefore, these modes stiffen the cp phase of DUT-8(Co) and DUT-8(Ni).

In general, the DUT-8(Ni) frequencies are higher, the DUT-8(Cu) frequencies are lower, and those of DUT-8(Co) are similar to DUT-8(Zn), which is the same observation that was made for the terahertz vibrations in the op phase.

In summary, the cp phase of DUT-8(Cu) is expected to be softer than DUT-8(Zn) because most of its terahertz vibrations have a lower frequency. Since such a DUT-8(Cu)_cp phase was not obtained experimentally yet, we will disregard this compound in further discussions. Analysing the softness of the Ni and Co variant is more difficult because some of the lowest frequency modes are softer, whereas modes involving translations and rotations of the 2,6-ndc linker are stiffer than in DUT-8(Zn). However, the softness of the latter modes in DUT-8(Zn) and DUT-8(Cu) might explain why their cp phase structure can easily transform to one with a disintegrated paddle wheel unit (see also next section). For modes above 75 cm^{-1}, it becomes hard to explain the observed frequency differences as there is no clear trend, the modes are more difficult to subdivide in contributions due to building blocks, and, related to that, not all modes of the four structures could be linked to each other (see Fig. S30†).

As the performed phonon calculations rely on the harmonic approximation, the predicted frequencies may be affected by anharmonicities. The calculation of anharmonic frequencies for the op and cp phases of DUT-8(Ni) (Section 9, ESI†) shows that the phonon modes in general do not soften when anharmonicities are taken into account, at least when phonon coupling is neglected. However, it remains an open question whether soft modes might be observed when also phonon coupling is considered.

2.3.3 Theoretical considerations about the effect of paddle wheel disintegration on terahertz vibrations. So far, our theoretical calculations considered only DUT-8(M) structures with an intact paddle wheel unit. However, as discussed in Section 2.2.2, the experimental cp phase structure of DUT-8(Zn) consists of a partially disintegrated paddle wheel unit, which is expected to have an impact on the lattice vibrations.

Static DFT calculations (see Section S6† for more details) suggest that the cp phases of DUT-8(Zn) and DUT-8(Cu) with disintegrated paddle wheels are more stable than the cp phases with an intact paddle wheel unit due to the increased dispersion interactions. In contrast, DUT-8(Ni) and DUT-8(Co) prefer intact paddle wheels (see Table 1). The theoretical predictions for the Zn, Ni, and Co variant are in line with the structures obtained experimentally. The Cu based compound experimentally shows complex behaviour: depending on the desolvation conditions, the compound remains in the op phase or collapses to the new phase, structurally differing from the cp phase.

The disintegration of the paddle wheel unit can affect the low-frequency modes, as they strongly depend on the interactions between the building blocks. This effect was investigated for the cp phase structure of DUT-8(Zn) (see Fig. S31† for visualization). The different morphology of the deformed and intact cp phase can give rise to other types of motion, complicating the identification of equivalent normal modes. Therefore, it was not possible to compare normal modes of the intact and deformed structure *via* the methodology using dot products explained in the theoretical section. Instead, 11 terahertz vibrations with the lowest non-zero frequencies in both structures were linked by visual inspection of the mode displacements (see Table S4†).

Based on the terahertz vibrations with the lowest frequencies, it is clear that, in general, the normal modes in the

Table 1 Electronic energy difference between the cp phases of DUT-8(M) with disintegrated (dis) and intact (int) paddle wheels (in kJ mol^{-1})

	Ni	Co	Zn	Cu
$\Delta E_{dis-int}$	122.24	33.06	−10.59	−25.57

deformed cp phase are red-shifted compared to those in the ideal cp phase. This could originate from the increased freedom of the dabco and 2,6-ndc linkers due to the breakage of the metal–oxygen bonds making the terahertz vibrations softer.

2.4 Spectroscopic characterization

To study the flexibility and mechanical properties of the DUT-8 materials, the frameworks were analysed using complementary analytical methods. Prior basic characterization of the crystal structures (Sections 2.1 and 2.2) will help to interpret the results and, where possible, the spectroscopic data will be linked with the theoretically predicted terahertz vibrations (Section 2.3).

2.4.1 Raman spectroscopy. Theoretical and experimental Raman spectra were compared to relate the theoretically predicted lattice vibrations of the model structures with the experiment.[37,41,50] For the op phase, a good agreement is observed between theory and experiment (see Fig. 6a and b).

In the high frequency range, Raman active bands arise due to local vibrations within the different building blocks, such as stretching within the carboxylate group, bending within the CH_2 groups, and stretching of the aromatic rings.

In the terahertz region (below 300 cm^{-1}) characterized by collective vibrations, one clear band around 20 cm^{-1} can be recognized, which is present in the spectra of all four op phase structures. This band can be assigned to a rotation of the 2,6-ndc linkers (see Fig. 3 and S17† and the modes highlighted in grey in Fig. 4 and 5). The exact values of the predicted and experimental frequencies of this Raman band for the four structures can be found in Table 2. The numbers reported earlier for DUT-8(Ni) are in good agreement with the present data.[51] The values for different metals are very close and, therefore, it is challenging to draw conclusions on the flexibility based on this single Raman band.

The Raman spectrum of the op phase of DUT-8(Ni) differs substantially from those of the other three structures. Around 1015 cm^{-1}, the band caused by C–C-stretching within the dabco unit is Raman active for DUT-8(Ni) (see Fig. S33†), while this is hardly the case for the other three structures. Furthermore, the

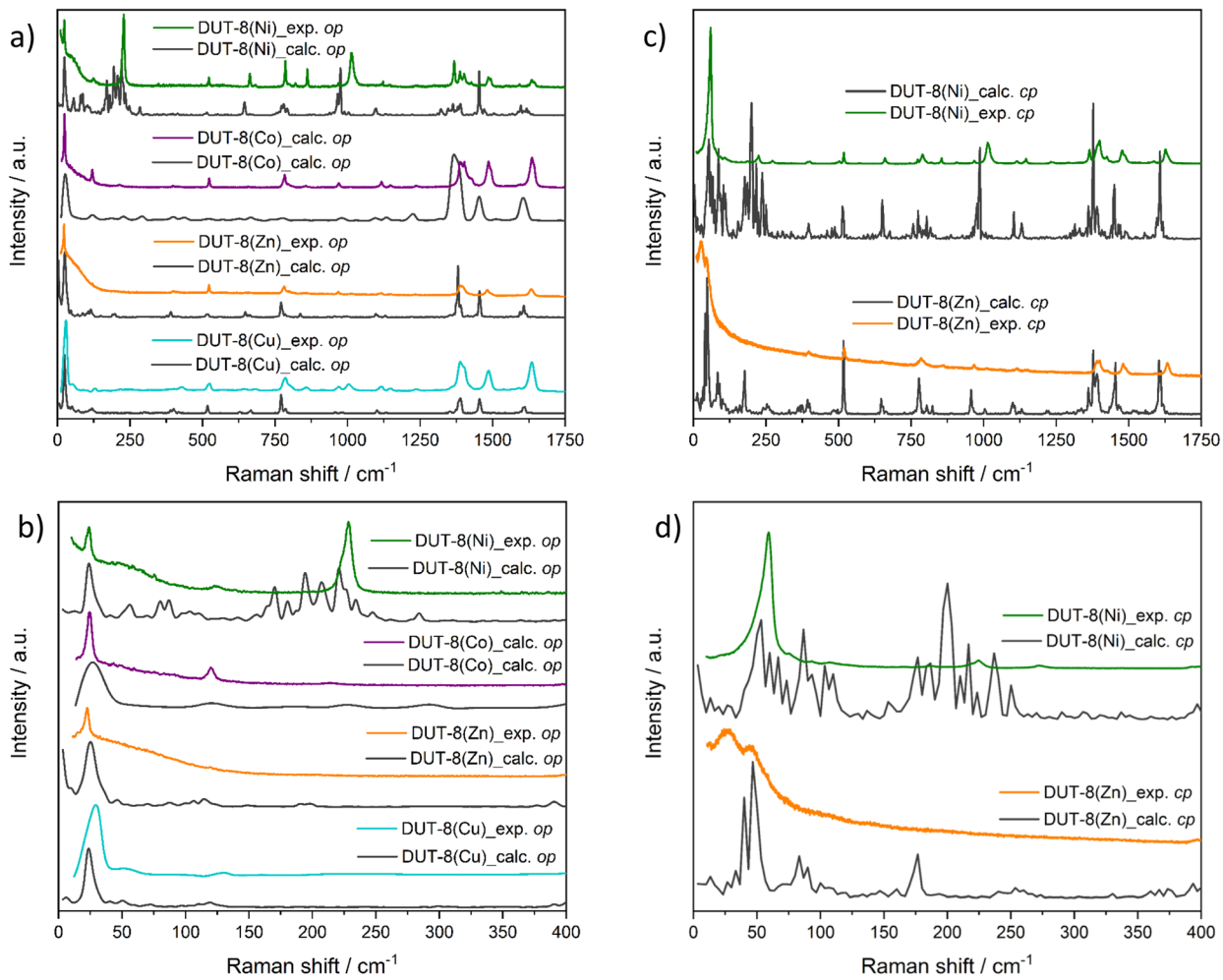

Fig. 6 Comparison of the calculated and measured Raman spectra for the op phases (a and b) and cp phases (c and d) of DUT-8(Ni),[50] DUT-8(Co),[41] DUT-8(Zn)[37] and DUT-8(Cu).[this work]

Table 2 Vibrational frequency (in cm^{-1}) of the Raman band due to 2,6-ndc linker rotation within the DUT-8(M) structures[a]

		Zn	Ni	Co	Cu
cp	Experiment	44 (ref. 37)	59 (ref. 50 and 51)	47 (ref. 41)	—
	Static DFT[This work]	60	72	70	57
	AIMD	47	52	NDA	53
	Static DFT[51]	NDA	67	NDA	NDA
op	Experiment	22 (ref. 37)	23 (ref. 50 and 51)	24 (ref. 41)	24[This work]
	Static DFT[This work]	21	16	16	19
	AIMD	25	24	27	24
	Static DFT[51]	NDA	25	NDA	NDA

[a] NDA – no data available.

distortion within the paddle wheel unit gives rise to an intense Raman band in the DUT-8(Ni) spectrum around 223 cm^{-1} (see Fig. S32†), which is absent in the spectra of the materials with other metals. Both characteristic vibrations are influenced by the paddle wheel structure and the coordinated dabco. From a geometry optimization with static DFT it is clear that the paddle wheel in the op phase structure of DUT-8(Ni) is distorted, whereas this is less the case for the other op phase structures (see Fig. S34† for a visualization).

For the cp phase structures, there is still a significant overlap between theoretically predicted Raman bands and experimental ones (see Fig. 6c and d). In the higher frequency region, the same bands appear that were present in the op phase structures but are slightly shifted.

In the terahertz region, it becomes clear that the strongest Raman band, corresponding to the rotation of the 2,6-ndc, is shifted to higher wavenumbers due to increased hindrance caused by the proximity of neighbouring linkers. Experimentally, the frequency of this band increases in the series from DUT-8(Zn) over DUT-8(Co) to DUT-8(Ni). The same trend follows from the static DFT calculations, although the theoretical frequencies seem to be overestimated. This probably results from an underestimation of the unit cell volume, which has been shown to largely affect the frequency of this mode in MIL-53(Al).[32,52] Based on this single Raman band, it appears that the cp phase of DUT-8(Zn) is softer than it is in Co and Ni based counterparts. One particular feature in the experimental Raman spectrum of DUT-8(Zn) that needs to be mentioned are the Raman bands at 26 and 44 cm^{-1}. Theoretically, only bands are predicted at 40–47 cm^{-1}. Considering that the experimental structure consists of a disintegrated paddle wheel (see Section 2.3.2), the additional Raman band at a lower frequency can be explained by the rotation of the 2,6-ndc linkers, which is less hindered.

2.4.2 Inelastic neutron scattering (INS). INS measurements were performed on the neutron time-of-flight (ToF) spectrometer NEAT at BER II in Berlin.[53,54] The ToF technique allows the study of dynamic phenomena in the materials and is sensitive to hydrogen modes due to the larger incoherent neutron cross section of hydrogen compared to other atoms. In neutron scattering experiments, in addition to scattering events with unchanged neutron energy (so-called elastic scattering), neutrons can lose or gain energy. Assuming that only phonon excitations are taking place in incoherently scattering systems, the dynamic structure factor can be described in the following form:

$$S(Q,\omega) = \delta(Q,\omega) \times e^{-2W(Q)} + S_{inc}(Q,\omega) \quad (1)$$

$$S_{inc}(Q,\omega) = \frac{Q^2 k_b T}{2M} e^{-2W(Q)} \frac{g(\omega)}{\omega^2} \quad (2)$$

where $e^{-2W(Q)}$ is the Debye–Waller factor, Q is the neutron momentum transfer, M is the effective mass of the scattering unit and $g(\omega)$ is the vibrational density of states. Due to the temperature dependence of the vibrational density of states, the neutron intensity on the neutron energy gain site depends strongly on temperature.

The energy range scanned in the experiments includes the low-frequency vibration region up to 121 cm^{-1}.

The spectra were collected for representative compounds containing Co, Cu, and Ni in the paddle wheel in the solvent-free, op forms at various temperatures, and for Co and Ni based MOFs in the cp form.

2.4.2.1 Open pore phases. To investigate the op forms, the samples in the submicron-sized particle range were synthesized to stabilize the metastable open pore solvent-free frameworks. For DUT-8(Ni)_op, the most pronounced peak is located at 3.2 meV (26 cm^{-1}) at 300 K (see Fig. 7a). The peak is visible in both the energy gain and energy loss regions. In accordance with the theoretical calculations, this vibration corresponds mainly to the rotation of the 2,6-ndc linkers in the structure (Fig. 8c and Table 3). The peak appears at the same position also in the spectra of DUT-8(Co)_op and DUT-8(Cu)_op, as is also predicted by theory. The second peak for DUT-8(Ni)_op is visible at 4.4 meV (36 cm^{-1}) in the spectrum at 300 K in the energy loss region. This peak mainly results from translations of hydrogen atoms on the 2,6-ndc linkers (so-called trampoline motion, Fig. 8d and Table 3). The positions of these two peaks do not change if the temperature is decreased to 39 K. At low temperatures (at 39 K), two additional peaks appear at 1.2 meV (9.6 cm^{-1}) and 2.1 meV (17 cm^{-1}) for DUT-8(Ni). Based on our calculations, the first peak involves rotations of the paddle wheel and dabco units together with translations of the 2,6-ndc linkers (Fig. 8a and Table 3).

The second peak involves rotations of the dabco pillars coupled with slight rotations of the paddle wheel units (Fig. 8b

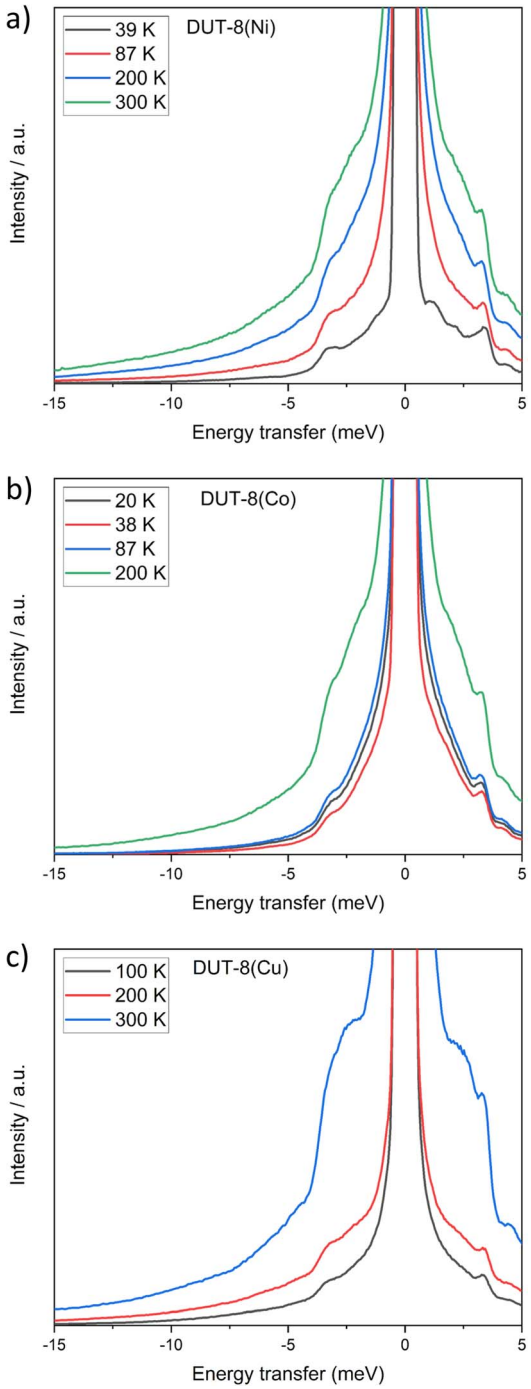

Fig. 7 Experimental INS spectra of DUT-8(Ni)_op (a), DUT-8(Co)_op (b) and DUT-8(Cu)_op (c) at different temperatures measured at 3 Å. The elastic line at $\omega = 0$ meV can be seen. The neutron energy gain site corresponds to the scattering with negative values of energy transfer, while neutron energy loss is related to the scattering at positive values of energy transfer.

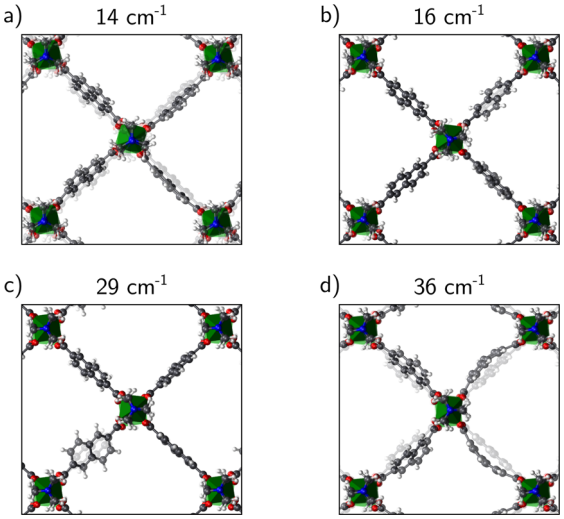

Fig. 8 (a) Rotations of paddle wheel and dabco units with translations of 2,6-ndc linkers. (b) Rotations of dabco units. (c) Rotations of 2,6-ndc linkers. (d) Trampoline motion of 2,6-ndc linkers.

and Table 3). Such peaks are not visible in the low-temperature spectra of DUT-8(Cu) and DUT-8(Co).

Comparison of the spectra for Ni, Co, and Cu based open pore phases at 200 K (Fig. 9b) shows close similarity. In all spectra, the peaks at 3.2 and 4.4 eV are present. For all investigated samples, the spectra are characterized by the increase of the signal at a very low energy range which cannot be resolved anymore from the elastic line.

The comparison of the quasi-elastic broadenings of the op phases shows the narrower peak for Cu and the broadest one for Co (Fig. 9b). However, with the increasing temperature, the quasi-elastic peak widths show a steep increase, indicative of accelerated motions (Fig. 7).

2.4.2.2 Closed pore phases. In the DUT-8(Ni)_cp phase, two peaks at 3.2 meV (25.8 cm^{-1}) and 7.5 meV (60 cm^{-1}) were observed in the energy loss region of the spectrum at 300 K (Fig. 10a). In the calculated data of DUT-8(Ni)_cp phase there are several modes between 13 and 43 cm^{-1} (modes A and B in Fig. 5). These modes often involve dabco rotations and may give rise to the peak at 3.2 meV. The lowering of the temperature causes a shift of the peak at 3.2 meV to the higher energies and at 38 K the peak is positioned at 3.5 meV (Fig. 9a).

The second peak observed at 7.5 meV can be assigned to phonon modes inducing 2,6-ndc linker rotations and is not visible at 38 K anymore.

For DUT-8(Co)_cp only one peak at 4.1 meV (33.1 cm^{-1}) could be identified in the experiment (Fig. 9a). The temperature dependence is not pronounced in this case and at 20 K the same position could be found (Fig. 10b). Obviously, the motion of the 2,6-ndc linker is influenced by the temperature and can be frozen in the cp phases. In contrast, the dabco rotation is still pronounced even at very low temperatures.

2.4.3 Phonon acoustic spectroscopy (PAS). Finally, we used ultrasonic pulse echo measurements to determine the speed of sound. To the best of our knowledge, this technique has rarely been used for the analysis of phonons in MOFs. A major challenge, however, is the necessity to prepare samples as highly dense pellets. As the op phases under high external pressure transform to the cp phase or deteriorate, we limited this study to the cp phases only. Due to the experimental densities of ≈80% (based on geometrical density), the measured values are expected to systematically underestimate the speed of sound but

Table 3 Calculated (static DFT) and observed positions of INS bands in the DUT-8(M)_op phases

Calculated for DUT-8(Ni), cm^{-1}	14	16–23	23–29	36–40
Experimental in DUT-8(M), cm^{-1}	9.6 (M = Ni)	17 (M = Ni)	26 (M = Ni, Co, Cu)	36 (M = Ni, Co, Cu)

allow a qualitative comparison between compounds.[55] In addition, the crystallinity of the samples suffers from pelletization and the PXRD of DUT-8(Co)_cp points on the considerable amorphization of the sample (Fig. S4c†).

We could tentatively observe a higher mean speed of sound for the Ni based system compared to Zn and Co (see Fig. 11), which have similar values, indicating that the Zn and Co based compounds have in overall a softer framework structures compared to DUT-8(Ni).

2.5 Comparison of complementary spectroscopic signatures of DUT-8 series

Table 4 compares the insights into collective motions obtained from the various spectroscopic techniques and the calculations. Despite some inabilities to exactly reproduce the observed peak positions by theory, tentative trends are well predicted.

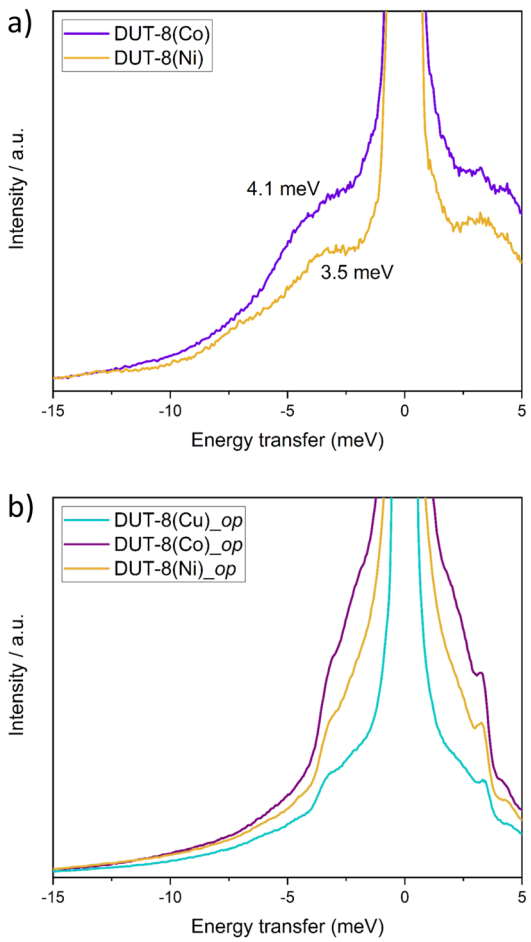

Fig. 9 (a) INS spectra of DUT-8(Ni)_cp and DUT-8(Co)_cp at 38 K and 20 K, respectively. (b) INS spectra of DUT-8(Ni)_op, DUT-8(Co)_op, and DUT-8(Cu)_op at 200 K.

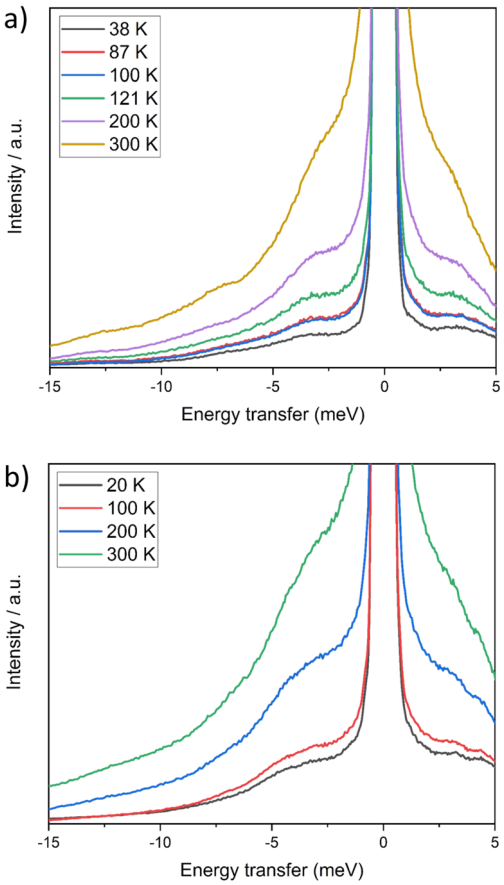

Fig. 10 INS spectra of DUT-8(Ni)_cp (a) and DUT-8(Co)_cp (b) at different temperatures measured at 3 Å.

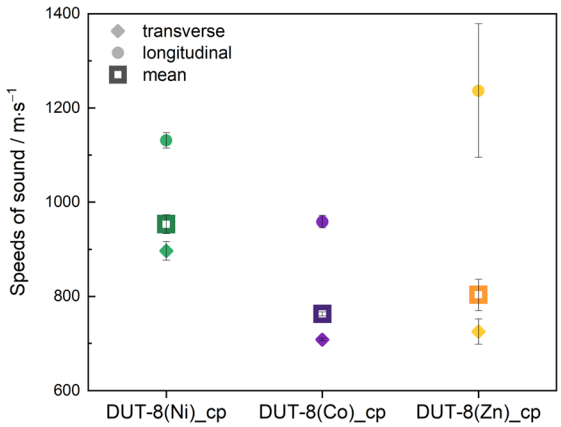

Fig. 11 Longitudinal, transverse and according mean speeds of sound in DUT-8(M)_cp (M = Ni, Co, Zn) at ≈80% density.

Table 4 Positions of characteristics peaks obtained by different methods[a]

	DUT-8(Ni)		DUT-8(Co)		DUT-8(Zn)		DUT-8(Cu)	
Samples/Methods	op	cp	op	cp	op	cp	op	cp
Calculated Raman bands/cm^{-1}								
Static DFT[This work]	16	72	16	70	21	60	19	57
AIMD	24	52	27	NDA	25	47	24	53
Static DFT[51]	25	67	NDA	NDA	NDA	NDA	NDA	NDA
Raman experimental bands/cm^{-1}								
Raman	23[b,d]	59	24[b,d]	47	22[b,d]	44 (26)	24[b,d]	—
INS experimental bands								
INS/cm^{-1} [meV]	9.6 [1.2] [c,e] 17 [2.1] 26 [3.2] 36 [4.4]	26 [3.2] 60 [7.5]	26 [3.2] [c,e] 36 [4.4]	33.1 [4.1]	NDA	NDA	26 [3.2] [d,e] 36 [4.4]	—
Speeds of sound/m s^{-1}								
PAS	NDA	953	NDA	762	NDA	803	NDA	—

[a] NDA – no data available. [b] Solvated with DMF. [c] Dried. [d] Macro-crystals. [e] Submicron crystals.

In particular, the increase in Raman frequencies of the Raman active phonon mode inducing linkers rotation as a result of op to cp transition, is reproduced both qualitatively and quantitatively. It is most pronounced for the Ni system but also obvious for Co and Zn. It hints at an increasing softness in the order Ni–Co–Zn for structures in their cp phase. PAS data tentatively support this claim. However, the observed trends are not so clear from INS data, but the INS peaks are also severely broadened for the cp phases.

The spectroscopic signatures of the op phases do not show significant differences.

Despite the above observations, it remains an open question to what extent these values can be applied to predict the softness of frameworks with respect to the op–cp phase transition. The spectra only reflect the elastic regime of the collective motions of all building blocks, which are in the terahertz region often related to the linker rotations. However, the trajectory for the inelastic phase transition may only for very small distortions resemble this elastic motion. For the phase transition, an additional activation barrier and the energy difference between op and cp forms will affect the phase transformation initiation and transformation rate.[56] Hence, the spectroscopic data can only give a tentative hint towards a better understanding of adsorption-induced phase transitions in flexible frameworks.

3 Conclusions

The pillared layer DUT-8 material is an important example of a switchable MOF exhibiting stimuli-responsive behaviour accompanied by a large change in unit cell volume. Low-frequency phonon modes can influence the dynamic response, which strongly depends on the choice of the metal ions forming the paddle wheel unit. In this study, we have applied multiple complementary spectroscopic techniques such as Raman spectroscopy, INS, and PAS combined with DFT calculations to unravel the vibrational properties of DUT-8(M) with different metal nodes (M = Ni, Co, Zn, Cu).

Theoretical Raman spectra were in good agreement with their experimental counterparts proving the validity of the model. They allowed pinpointing the single characteristic Raman band in the terahertz range as a phonon mode inducing a rotation of the 2,6-ndc linker around its axis. This Raman band has a comparably low frequency in the op phases of the different DUT-8(M) structures. When the framework transforms from the op to the cp phase, this mode increases significantly in frequency. This increase was most pronounced in the Ni based material, suggesting that it has the stiffest cp phase structure, which was also supported by phonon acoustic spectroscopy data.

INS spectroscopy gave insight in the temperature dependent behaviour of the linker modes, showing that the motion of the 2,6-ndc linker is influenced by the temperature and can be frozen in the cp phase.

Although it was not possible to capture the inelastic barriers affecting the phase transition, the spectroscopic data reported in this study provide valuable insight into the elastic deformations of the building blocks and their cooperative motions affecting the observed flexibility in DUT-8(M) materials, promoting the mechanistic understanding of guest induced phase transition in switchable MOFs.

4 Experimental

4.1 Materials

$Ni(NO_3)_2 \cdot 6H_2O$ (99%), $Co(NO_3)_2 \cdot 6H_2O$ (99%), $Zn(NO_3)_2 \cdot 6H_2O$ (99%), $Cu(NO_3)_2 \cdot 3H_2O$ (99–104%), 2,6-H_2ndc (99%), dabco (99%) were purchased from Sigma Aldrich. All solvents were at least of analytical grade, purchased from commercial suppliers and used without further purification.

4.2 MOF synthesis and desolvation

The isomorphous DUT-8(M) compounds (M = Ni, Co, Zn, Cu) were synthesized according to procedures reported earlier or following a slightly modified protocol.

4.2.1 Samples for INS

4.2.1.1 Synthesis of macro-sized crystals. The macro-sized crystals (Table S1†) were synthesized following the modified procedures described in ref. 40, 41, and 46.

DUT-8(Co):[41] $Co(NO_3)_2 \cdot 6H_2O$ (1.687 g, 5.81 mmol, 1.56 eq.) were dissolved in 35 mL DMF, 2,6-H_2ndc (1.249, 5.81 mmol, 1.56 eq.) in 105 mL DMF, and dabco (0.420 g, 3.75 mmol, 1 eq.) in 35 mL DMF using ultrasound treatment and combined. Subsequently, the mixture was transferred into Teflon vessels and heated at 393 K in autoclaves for 48 h. After cooling to room temperature (RT), the sample was washed several times with DMF. This synthesis procedure results in differently sized crystals, therefore larger crystals were separated from smaller ones and only large crystals (9–25 μm, Fig. S3b†) were used for the measurements.

DUT-8(Ni):[40] all chemicals were dissolved separately: $Ni(NO_3)_2 \cdot 6H_2O$ (814 mg, 2.8 mmol, 1.6 eq.) in 12 mL DMF, 2,6-H_2ndc (606 mg, 2.8 mmol, 1.6 eq.) in 30 mL DMF, and dabco (201 mg, 1.8 mmol, 1 eq.) in 18 mL methanol. The mixture was sonicated for 10 min, transferred into Teflon vessels (50 mL) and heated in an autoclaves at 393 K for 48 h. After cooling to RT the product was isolated by decanting the mother liquor and washed with fresh DMF.

DUT-8(Cu):[46] $Cu(NO_3)_2 \cdot 3H_2O$ (1.450 g, 6 mmol, 1 eq.) and dabco (0.673 g, 6 mmol, 1 eq.) were dissolved in 30 mL and 22.5 mL MeOH, respectively. 2,6-H_2ndc (1.297 g, 6 mmol, 1 eq.) was dissolved in 67.5 mL DMF. Clear solutions of the copper salt and 2,6-H_2ndc linker were mixed with subsequent addition of 135 mL DMF. Then 13 mL of 1 M HCl was added to the mixture dropwise. Afterwards, dabco was added, and the reaction mixture was distributed between several Pyrex tubes, which were placed into the oven at 353 K for 48 hours. The resulting crystals were washed three times with DMF.

4.2.1.2 Desolvation of macro-sized crystals. In the following treatment procedure, DMF used in the synthesis of DUT-8(M) was exchanged for a lower boiling point solvents. The macro-sized crystals of DUT-8(Ni), and DUT-8(Co) were washed during 3 days with dichloromethane (DCM), while DUT-8(Cu) sample was washed with ethanol. After solvent exchange, samples were filtered under argon flow. DUT-8(Cu), DUT-8(Co) samples were evacuated at 423 K, and DUT-8(Ni) was evacuated at RT during 16 h.

4.2.1.3 Synthesis of submicron-sized samples. The submicron-sized crystals were synthesized following the modified procedures described in ref. 40 and 41.

DUT-8(Co):[41] 2,6-H_2ndc (1.249 g, 5.7 mmol, 1 eq.) was dissolved in 126 mL DMF, $Co(NO_3)_2 \cdot 6H_2O$ (1.678 mg, 5.7 mmol, 1 eq.) was dissolved in 42 mL DMF, dabco was dissolved in (2.1 g, 18.7 mmol, 3.2 eq.) in 42 mL DMF. Three solutions were combined, forming the cloudy mixture, which was exposed to ultrasound treatment for 60 minutes. The supernatant was removed by centrifugation and crystals were washed with DMF several times.

DUT-8(Ni):[40] chemicals were dissolved separately: 2,6-H_2ndc (2.94 g, 13.7 mmol, 1 eq.) in 200 mL DMF, $Ni(NO_3)_2 \cdot 6H_2O$ (4.34 g, 15 mmol, 1.1 eq.) in 50 mL DMF, dabco (3.36 g, 30 mmol, 2.2 eq.) in 50 mL DMF. The clear solution of nickel salt was added to the linker solution. Afterwards, dabco was added to the reaction mixture. The resulting cloudy mixture was then treated in an ultrasonic bath for 50 minutes. The supernatant was removed by centrifugation, and the crystals were washed with DMF several times.

4.2.1.4 Desolvation of submicron-sized crystals. DUT-8(Co) crystals were desolvated directly from DMF by heating in vacuum at 423 K. Prior to solvent removal, the DMF in the pores of DUT-8(Ni) was exchanged to DCM during 3 days. The sample was filtered under argon flow and evacuated for 16 h at RT.

4.2.2 Samples for phonon acoustic spectroscopy

4.2.2.1 Macro-sized samples. DUT-8(Zn):[38] typically, $Zn(NO_3)_2 \cdot 6H_2O$ (312 mg, 1.05 mmol, 1.7 eq.) was dissolved in 5 mL DMF, 2,6-H_2ndc (227 mg, 1.05 mmol, 1.7 eq.) was dissolved in 20 mL DMF, and dabco (70 mg, 0.625 mmol, 1 eq.) was dissolved in 5 mL DMF using ultrasound treatment during 10 min. The three resulting solutions were slowly mixed and heated in an oven at 353 K for 17 min. After the pre-treatment, the solution was placed into Pyrex tubes and heated at 393 K for 48 hours. After cooling to room temperature, the crystals were washed several times with DMF.

DUT-8(Co):[41] all chemicals were dissolved separately: $Co(NO_3)_2 \cdot 6H_2O$ (241 mg, 0.83 mmol, 1.56 eq.) in 5 mL DMF, 2,6-H_2ndc (178.5 mg, 0.83 mmol, 1.56 eq.) in 15 mL DMF and dabco (60 mg, 0.53 mmol, 1 eq.) in 5 mL DMF using ultrasound treatment. Subsequently all solutions were combined, the mixture was transferred into a Teflon vessel (50 mL) and heated at 393 K in an autoclave for 48 h. After cooling to room temperature, the sample was washed several times with DMF.

DUT-8(Ni): sample was synthesized and desolvated according to procedure reported earlier.[40] Afterwards, the desolvated crystals were subjected to recrystallization step, leading to the more uniform crystal size distribution (Fig. S5a†). For it, 210 mg of sample was placed into the mixture containing 210 mL DMF and 90 mL MeOH, and heated at 353 °C in oven during 120 h. After cooling to room temperature, the sample was washed several times with DMF.

4.2.2.2 Desolvation of macro-sized crystals. The macro-sized crystals of DUT-8(Co), DUT-8(Zn), and DUT-8(Ni) were washed with DCM during 3 days. After solvent exchange, samples were filtered under argon flow. DUT-8(Co) and DUT-8(Zn) samples were evacuated at 423 K, DUT-8(Ni) sample was evacuated at 393 K for 16 h.

4.2.3 Sample for Raman spectroscopy. DUT-8(Cu):[46] $Cu(NO_3)_2 \cdot 3H_2O$ (0.9664 g, 4 mmol, 1 eq.) and dabco (0.4496 g, 4 mmol, 1 eq.) were dissolved under ultrasonication in 20 mL DMF and 15 mL MeOH, respectively. 2,6-H_2ndc (1.7292 g, 8 mmol, 2 eq.) was dissolved in 128 mL DMF. Clear solutions of the copper salt and linker were mixed and 8.8 mL of 1 M HCl was added to the mixture dropwise. Subsequently, dabco was added and the cloudy suspension was distributed between several Pyrex tubes and placed into a preheated oven. After 10 min at 353 K, the tubes were taken out, and the white

precipitate formed was removed by centrifugation. The clear solution was placed again into the oven at 353 K for 48 hours. The resulting turquoise crystals were washed with DMF at least 3 times.

5 Analytical methods

5.1 Powder X-ray diffraction (PXRD)

PXRD patterns were measured at room temperature on a STOE STADI P diffractometer using Cu-Kα1 radiation (λ = 1.5406 Å) and a 2D detector (Mythen, Dectris). All measurements were performed in transmission geometry using a rotating flatbed sample holder, 2θ resolution of 0.015° in a step scanning mode with 6° steps and exposition time of 120 s per step.

5.2 Phonon acoustic spectroscopy

For pulse-echo speed of sound measurements, the DUT-8(M) (M = Ni, Co, Zn) powder samples were pressed into blanks by manual pressing and further densified by isostatic pressing for 45 min at 360 MPa, under the exclusion of air. The obtained pellets (~1.15 mm thickness, 9.15 mm diameter and a mass of ~100 mg) of 78% to 80% density were then coated with a 200 nm thick protective layer of Au by thermal evaporation. Those pellets were analysed using an EPOCH 600 (OLYMPUS) in nitrogen atmosphere. Therefore, piezoelectric transducers (5 MHz) for longitudinal and transverse signals were acoustically coupled to the pellet with honey as agent, hence the protective Au layer. The times between reflected ultrasonic pulses were monitored and related to speeds of sounds by the measured pellet thickness. The mean speed of sound (v_{mean}) was calculated from the transverse and longitudinal (v_{trans} and v_{long}) speeds of sound *via* eqn (3).

$$(v_{mean})^3 = \frac{3}{v_{long}{}^{-3} + 2v_{trans}{}^{-3}} \quad (3)$$

The reported values reflect averages with standard deviations for uncertainties of three equally prepared and analysed pellets of every compound. In DUT-8(Zn) only two transverse responses could be reliably interpreted. The triplicates show reproducibility and include possible variations in microstructure, which, due to the limited pellet density, overall leads to a systematic underestimate of the speed of sound.

5.3 Inelastic neutron scattering

INS measurements were performed at Helmholtz Zentrum Berlin (BER II) on the neutron time-of-flight (ToF) spectrometer NEATII[54] with an incident neutron wavelength of 3 Å. A cylindrical sample holder cell made of aluminium and with an inner cylinder (the outer diameter of the sample was 1.02 cm and the inner diameter of the sample was 0.555 cm) was used. The mass of dry samples used for the measurements was in the range of 0.5–0.7 g. The sample preparation was carried out under inert gas atmosphere in the glove box. Before the measurements, the samples were evacuated at 50 °C. Measurements with vanadium and empty sample holders were performed to correct for experimental distortions and for the background contribution. Data reduction, which included normalization with vanadium, corrections for detector efficiency and subtraction of background, was performed with MANTID software packages.[57]

5.4 Raman spectroscopy

Raman spectra of DUT-8(Cu)_op were collected by using a S&I Monovista CRS + Raman spectrometer with 514 nm DPSS laser (Hübner photonics) and a Bragg grating for measuring in the low frequency region. The laser was aligned and then focused on the sample using an Olympus 20× objective at a laser power of ≈0.1 mW with an exposure time of 100 seconds. Spectra were calibrated with respect to the Raman spectrum of toluene.

6 Theoretical calculations

6.1 Static density functional theory (DFT)

Periodic density functional theory calculations were performed with the Vienna *Ab initio* Simulation Package (VASP).[58–60] The PBE functional[61] was chosen, including Grimme's D3 dispersion[62] with Becke-Johnson damping,[63] which has proven to yield accurate vibrational spectra for similar systems.[32,52] A projector-augmented plane-wave basis set[64] with a plane-wave cut-off of 600 eV was adopted. A different Monkhorst–Pack *k*-mesh[65] was employed for the op and cp phases of DUT-8. For calculations on the op phase, the *k*-mesh was set to 2 × 2 × 4, whereas the *k*-mesh was enlarged to 4 × 2 × 4 for structures in the cp phase. The SCF cycle of the electronic structure calculations was considered to be converged when the energy difference between subsequent steps became lower than 10^{-10} eV. For the structures with magnetic Ni, Co, and Cu atoms, simulations were performed in the ferromagnetic spin state.

Theoretical equilibrium structures of the DUT-8 materials were obtained after optimization of the geometry. For each structure, the volume–energy equation of state was first constructed from several fixed volume optimizations in which both the ions and cell shape were allowed to relax. These optimizations were stopped when the energy difference between the two subsequent steps became lower than 10^{-9} eV. The optimal unit cell volume was determined *via* a Rose–Vinet fit to the equation of state, and a final fixed volume optimization was performed at this optimal volume.

The Hessian was calculated at the equilibrium geometry following a finite difference approach in which the ions are displaced separately along the three Cartesian directions with an amplitude of ±0.015 Å. The normal modes and corresponding frequencies were obtained *via* a normal mode analysis using TAMkin.[66] IR intensities of these modes were determined by making use of Born effective charges calculated *via* density functional perturbation theory.[67,68] The analysis of the normal modes of the different structures required additional characterization. Firstly, to compare vibrational frequencies of equivalent normal modes between different structures, the dot product of the orthonormal mass-weighted normal modes was calculated. Two modes were considered of the same type when the square of their dot product was larger than 0.25. Secondly, each mass-weighted normal mode was subdivided in

contributions due to translations and rotations of the 2,6-ndc linker, the dabco linker and the paddle wheel unit. For that purpose, the inertia tensor was constructed for each building block, and mass-weighted translations and rotations of each building block were defined along the principal axes of each building block. The square of the dot product of a translation or rotation of a building block with the mass-weighted normal mode of interest defines the magnitude of the contribution of that type of motion to the normal mode.

6.2 *Ab initio* molecular dynamics (AIMD)

Ab initio molecular dynamics simulations were performed with the CP2K software at the same level of theory as the VASP calculations (PBE-D3(BJ)) using the Quickstep module.[69] The Gaussian plane wave method was adopted, combining atom-centered Gaussian orbitals with auxiliary plane waves.[70] The TZVP-MOLOPT basis set was chosen for the atomic basis set,[71] making additional use of GTH pseudopotentials to describe the core electrons.[72] The cut-off and relative cut-off of the plane wave basis set were set to 1000 Ry and 60 Ry, respectively. All simulations were executed at the gamma point. The SCF cycle of each MD step was considered to be converged when the energy was lower than 10^{-6} Ha. For the structures with magnetic Ni, Co, and Cu atoms, simulations were performed in the ferromagnetic spin state.

AIMD simulations were run in the NVT ensemble starting from the statically optimized structure. In the NVT ensemble, the volume and cell shape remain fixed, but the ions are allowed to move. Moreover, the temperature of 300 K was controlled using a Nosé–Hoover chain thermostat with five beads and a time constant of 100 fs. Each structure was equilibrated for 5 ps followed by a production run of 10 ps with a time step of 0.5 fs. The prediction of the Raman spectrum of a given MD trajectory requires the calculation of the polarizability tensor at subsequent time steps. The polarizability tensor can be obtained from the dipole moment with and without an electric field by a finite difference approach.[73] The Raman spectrum is retrieved from a trajectory of polarizability tensors by taking the Fourier transform of specific autocorrelation functions.[73] To ensure that the spectra were predicted in the complete IR range, dipole moments were calculated every 2 fs (every 4th MD step). According to the above procedure, theoretical Raman spectra could be calculated for DUT-8(Zn), DUT-8(Cu), and DUT-8(Ni). The calculation of dipole moments in the trajectories of DUT-8(Co) proved to be problematic because of its high spin state. The calculation of the dipole moments did not converge for the trajectory in the cp phase, whereas it did converge for only a small part of the trajectory in the op phase. Therefore, the Raman spectrum of the cp phase could not be calculated and the Raman spectrum of the op phase was taken for a trajectory of only 2.5 ps.

Data availability

All the data containing the input structures and scripts for the simulations can be accessed *via* **https://github.com/AlexanderHoffman/supporting-info**.

Author contributions

I. S., S. K, V. V. S. – conceptualization, I. S., A. H., S. K., V. B., V. G. – formal analysis, I. S., V. V. S., S. K. – funding acquisition, A. H., S. K., L. A., V. B., V. G., M. R. – investigation, I. S., S. K., V. V. S. – project administration, M. R., V. S., S. K. – validation, A. H., I. S., L. A., S. K. – writing – original draft, all – writing, review & editing.

Conflicts of interest

There are no conflicts to declare.

Acknowledgements

This work is financially supported by DFG (Deutsche Forschungsgemeinschaft) under contracts FOR 2433 and within the project with number 448809307. The neutron source BER II of HZB is gratefully acknowledged for the allocation of neutron scattering beamtime on NEAT instrument. We thank Mariia Maliuta and Dr Sebastian Ehrling for their support in sample preparation. V. V. S. acknowledges funding from the Fund for Scientific Research Flanders (FWO) and the Research Board of Ghent University (BOF). The computational resources and services used in this work were provided by the Flemish Supercomputer Center (VSC), funded by FWO and the Flemish Government.

References

1 S. Krause, N. Hosono and S. Kitagawa, *Angew. Chem., Int. Ed.*, 2020, **59**, 15325.
2 F. Bigdeli, C. T. Lollar, A. Morsali and H.-C. Zhou, *Angew. Chem., Int. Ed.*, 2020, **59**, 4652.
3 S. K. Elsaidi, M. H. Mohamed, D. Banerjee and P. K. Thallapally, *Coord. Chem. Rev.*, 2018, **358**, 125.
4 N. Aljammal, C. Jabbour, S. Chaemchuen, T. Juzsakova and F. Verpoort, *Catalysts*, 2019, **9**, 512.
5 Q. Dong, X. Zhang, S. Liu, R.-B. Lin, Y. Guo, Y. Ma, A. Yonezu, R. Krishna, G. Liu, J. Duan, R. Matsuda, W. Jin and B. Chen, *Angew. Chem., Int. Ed.*, 2020, **59**, 22756.
6 S. Yuan, L. Zou, H. Li, Y.-P. Chen, J. Qin, Q. Zhang, W. Lu, M. B. Hall and H.-C. Zhou, *Angew. Chem., Int. Ed.*, 2016, **55**, 10776.
7 P. Horcajada, C. Serre, G. Maurin, N. A. Ramsahye, F. Balas, M. Vallet-Regí, M. Sebban, F. Taulelle and G. Férey, *J. Am. Chem. Soc.*, 2008, **130**, 6774.
8 R. Freund, O. Zaremba, G. Arnauts, R. Ameloot, G. Skorupskii, M. Dincă, A. Bavykina, J. Gascon, A. Ejsmont, J. Goscianska, M. Kalmutzki, U. Lächelt, E. Ploetz, C. S. Diercks and S. Wuttke, *Angew. Chem., Int. Ed.*, 2021, **60**, 23975.
9 W. Cai, J. Wang, C. Chu, W. Chen, C. Wu and G. Liu, *Adv. Sci.*, 2019, **6**, 1801526.
10 J.-P. Zhang, H.-L. Zhou, D.-D. Zhou, P.-Q. Liao and X.-M. Chen, *Natl. Sci. Rev.*, 2017, **5**, 907.

11 I. M. Walton, J. M. Cox, J. A. Coppin, C. M. Linderman, D. G. Patel and J. B. Benedict, *Chem. Commun.*, 2013, **49**, 8012.
12 Y. Kim, R. Haldar, H. Kim, J. Koo and K. Kim, *Dalton Trans.*, 2016, **45**, 4187.
13 A. Krylov, I. Senkovska, S. Ehrling, M. Maliuta, S. Krylova, E. Slyusareva, A. Vtyurin and S. Kaskel, *Chem. Commun.*, 2020, **56**, 8269.
14 M. Wei, Y. Wan and X. Zhang, *J. Compos. Sci.*, 2021, **5**, 101.
15 Z. Liu, L. Zhang and D. Sun, *Chem. Commun.*, 2020, **56**, 9416.
16 B. Kuchta, F. Formalik, J. Rogacka, A. V. Neimark and L. Firlej, *Z. Kristallogr. – Cryst. Mater.*, 2019, **234**, 513.
17 A. E. J. Hoffman, I. Senkovska, J. Wieme, A. Krylov, S. Kaskel and V. Van Speybroeck, *J. Mater. Chem. A*, 2022, **10**, 17254.
18 F. Formalik, M. Fischer, J. Rogacka, L. Firlej and B. Kuchta, *Microporous Mesoporous Mater.*, 2020, **304**, 109132.
19 F. Formalik, B. Mazur, M. Fischer, L. Firlej and B. Kuchta, *J. Phys. Chem. C*, 2021, **125**, 7999.
20 N. C. Burtch, J. Heinen, T. D. Bennett, D. Dubbeldam and M. D. Allendorf, *Adv. Mater.*, 2018, **30**, 1704124.
21 T. Kamencek, N. Bedoya-Martínez and E. Zojer, *Phys. Rev. Mater.*, 2019, **3**, 116003.
22 K. Yang, G. Zhou and Q. Xu, *RSC Adv.*, 2016, **6**, 37506.
23 I. E. Collings and A. L. Goodwin, *J. Appl. Phys.*, 2019, **126**, 181101.
24 S. Henke, W. Li and A. K. Cheetham, *Chem. Sci.*, 2014, **5**, 2392.
25 J. C. Tan and A. K. Cheetham, *Chem. Soc. Rev.*, 2011, **40**, 1059.
26 J.-C. Tan, B. Civalleri, C.-C. Lin, L. Valenzano, R. Galvelis, P.-F. Chen, T. D. Bennett, C. Mellot-Draznieks, C. M. Zicovich-Wilson and A. K. Cheetham, *Phys. Rev. Lett.*, 2012, **108**, 095502.
27 S. A. Moggach, T. D. Bennett and A. K. Cheetham, *Angew. Chem., Int. Ed.*, 2009, **48**, 7087.
28 A. U. Ortiz, A. Boutin, A. H. Fuchs and F.-X. Coudert, *J. Phys. Chem. Lett.*, 2013, **4**, 1861.
29 A. U. Ortiz, A. Boutin, A. H. Fuchs and F.-X. Coudert, *Phys. Rev. Lett.*, 2012, **109**, 195502.
30 M. R. Ryder, B. Civalleri, T. D. Bennett, S. Henke, S. Rudić, G. Cinque, F. Fernandez-Alonso and J.-C. Tan, *Phys. Rev. Lett.*, 2014, **113**, 215502.
31 M. T. Ruggiero, *J. Infrared Millim. Terahertz Waves*, 2020, **41**, 491.
32 A. E. J. Hoffman, L. Vanduyfhuys, I. Nevjestić, J. Wieme, S. M. J. Rogge, H. Depauw, P. Van Der Voort, H. Vrielinck and V. Van Speybroeck, *J. Phys. Chem. C*, 2018, **122**, 2734.
33 N. Klein, H. C. Hoffmann, A. Cadiau, J. Getzschmann, M. R. Lohe, S. Paasch, T. Heydenreich, K. Adil, I. Senkovska, E. Brunner and S. Kaskel, *J. Mater. Chem.*, 2012, **22**, 10303.
34 N. Klein, C. Herzog, M. Sabo, I. Senkovska, J. Getzschmann, S. Paasch, M. R. Lohe, E. Brunner and S. Kaskel, *Phys. Chem. Chem. Phys.*, 2010, **12**, 11778.
35 V. Bon, N. Klein, I. Senkovska, A. Heerwig, J. Getzschmann, D. Wallacher, I. Zizak, M. Brzhezinskaya, U. Mueller and S. Kaskel, *Phys. Chem. Chem. Phys.*, 2015, **17**, 17471.
36 S. Ehrling, M. Mendt, I. Senkovska, J. D. Evans, V. Bon, P. Petkov, C. Ehrling, F. Walenszus, A. Pöppl and S. Kaskel, *Chem. Mater.*, 2020, **32**, 5670.
37 L. Abylgazina, I. Senkovska, S. Ehrling, V. Bon, P. St. Petkov, J. D. Evans, S. Krylova, A. Krylov and S. Kaskel, *CrystEngComm*, 2021, **23**, 538.
38 L. Abylgazina, I. Senkovska, R. Engemann, S. Ehrling, T. E. Gorelik, N. Kavoosi, U. Kaiser and S. Kaskel, *Front. Chem.*, 2021, **9**, 674566.
39 H. Miura, V. Bon, I. Senkovska, S. Ehrling, S. Watanabe, M. Ohba and S. Kaskel, *Dalton Trans.*, 2017, **46**, 14002.
40 N. Kavoosi, V. Bon, I. Senkovska, S. Krause, C. Atzori, F. Bonino, J. Pallmann, S. Paasch, E. Brunner and S. Kaskel, *Dalton Trans.*, 2017, **46**, 4685.
41 S. Ehrling, I. Senkovska, V. Bon, J. D. Evans, P. Petkov, Y. Krupskaya, V. Kataev, T. Wulf, A. Krylov, A. Vtyurin, S. Krylova, S. Adichtchev, E. Slyusareva, M. S. Weiss, B. Büchner, T. Heine and S. Kaskel, *J. Mater. Chem. A*, 2019, **7**, 21459.
42 M. Rauche, S. Ehrling, S. Krause, I. Senkovska, S. Kaskel and E. Brunner, *Chem. Commun.*, 2019, **55**, 9140.
43 S. Ehrling, E. M. Reynolds, V. Bon, I. Senkovska, T. E. Gorelik, J. D. Evans, M. Rauche, M. Mendt, M. S. Weiss, A. Pöppl, E. Brunner, U. Kaiser, A. L. Goodwin and S. Kaskel, *Nat. Chem.*, 2021, **13**, 568.
44 L. Bondorf, J. L. Fiorio, V. Bon, L. Zhang, M. Maliuta, S. Ehrling, I. Senkovska, J. D. Evans, J.-O. Joswig, S. Kaskel, T. Heine and M. Hirscher, *Sci. Adv.*, 2022, **8**, eabn7035.
45 H. Miura, V. Bon, I. Senkovska, S. Ehrling, N. Bönisch, G. Mäder, S. Grünzner, A. Khadiev, D. Novikov, K. Maity, A. Richter and S. Kaskel, *Adv. Mater.*, 2023, **35**, 2207741.
46 M. Maliuta, I. Senkovska, R. Thümmler, S. Ehrling, S. Becker, V. Romaka, V. Bon, J. D. Evans and S. Kaskel, *Dalton Trans.*, 2023, **52**, 2816.
47 K. A. H. Alzahrani and R. J. Deeth, *Dalton Trans.*, 2016, **45**, 11944.
48 J. Wieme, K. Lejaeghere, G. Kresse and V. Van Speybroeck, *Nat. Commun.*, 2018, **9**, 4899.
49 M. R. V. Jørgensen, S. Cenedese, H. F. Clausen, J. Overgaard, Y.-S. Chen, C. Gatti and B. B. Iversen, *Inorg. Chem.*, 2013, **52**, 297.
50 A. Krylov, A. Vtyurin, P. Petkov, I. Senkovska, M. Maliuta, V. Bon, T. Heine, S. Kaskel and E. Slyusareva, *Phys. Chem. Chem. Phys.*, 2017, **19**, 32099.
51 A. Krylov, I. Yushina, E. Slyusareva, S. Krylova, A. Vtyurin, S. Kaskel and I. Senkovska, *Phys. Chem. Chem. Phys.*, 2022, **24**, 3788.
52 A. E. J. Hoffman, J. Wieme, S. M. J. Rogge, L. Vanduyfhuys and V. Van Speybroeck, *Z. Kristallogr. – Cryst. Mater.*, 2019, **234**, 529.
53 M. Russina, G. Guenther, V. Grzimek, R. Gainov, M.-C. Schlegel, L. Drescher, T. Kaulich, W. Graf, B. Urban, A. Daske, K. Grotjahn, R. Hellhammer, G. Buchert, H. Kutz, L. Rossa, O.-P. Sauer, M. Fromme, D. Wallacher, K. Kiefer, B. Klemke, N. Grimm, S. Gerischer, N. Tsapatsaris and K. Rolfs, *Physica B Condens. Matter*, 2018, **551**, 506.

54 G. Günther and M. Russina, *Nucl. Instrum. Methods Phys. Res., Sect. B*, 2016, **828**, 250.
55 S. Hirooka and M. Kato, *J. Nucl. Sci. Technol.*, 2018, **55**, 356.
56 S. Ehrling, H. Miura, I. Senkovska and S. Kaskel, *Trends Chem.*, 2021, **3**, 291.
57 O. Arnold, J. C. Bilheux, J. M. Borreguero, A. Buts, S. I. Campbell, L. Chapon, M. Doucet, N. Draper, R. Ferraz Leal, M. A. Gigg, V. E. Lynch, A. Markvardsen, D. J. Mikkelson, R. L. Mikkelson, R. Miller, K. Palmen, P. Parker, G. Passos, T. G. Perring, P. F. Peterson, S. Ren, M. A. Reuter, A. T. Savici, J. W. Taylor, R. J. Taylor, R. Tolchenov, W. Zhou and J. Zikovsky, *Nucl. Instrum. Methods Phys. Res., Sect. B*, 2014, **764**, 156.
58 G. Kresse and J. Hafner, *Phys. Rev. B: Condens. Matter Mater. Phys.*, 1993, **47**, 558.
59 G. Kresse and J. Furthmüller, *Comput. Mater. Sci.*, 1996, **6**, 15.
60 G. Kresse and J. Furthmüller, *Phys. Rev. B: Condens. Matter Mater. Phys.*, 1996, **54**, 11169.
61 J. P. Perdew, K. Burke and M. Ernzerhof, *Phys. Rev. Lett.*, 1996, **77**, 3865.
62 S. Grimme, *J. Comput. Chem.*, 2006, **27**, 1787.
63 S. Grimme, S. Ehrlich and L. Goerigk, *J. Comput. Chem.*, 2011, **32**, 1456.
64 P. E. Blöchl, *Phys. Rev. B: Condens. Matter Mater. Phys.*, 1994, **50**, 17953.
65 H. J. Monkhorst and J. D. Pack, *Phys. Rev. B: Solid State*, 1976, **13**, 5188.
66 A. Ghysels, T. Verstraelen, K. Hemelsoet, M. Waroquier and V. Van Speybroeck, *J. Chem. Inf. Model.*, 2010, **50**, 1736.
67 S. Baroni and R. Resta, *Phys. Rev. B: Condens. Matter Mater. Phys.*, 1986, **33**, 7017.
68 M. Gajdoš, K. Hummer, G. Kresse, J. Furthmüller and F. Bechstedt, *Phys. Rev. B: Condens. Matter Mater. Phys.*, 2006, **73**, 045112.
69 T. D. Kühne, M. Iannuzzi, M. D. Ben, V. V. Rybkin, P. Seewald, F. Stein, T. Laino, R. Z. Khaliullin, O. Schütt, F. Schiffmann, D. Golze, J. Wilhelm, S. Chulkov, M. H. Bani-Hashemian, V. Weber, U. Borštnik, M. Taillefumier, A. S. Jakobovits, A. Lazzaro, H. Pabst, T. Müller, R. Schade, M. Guidon, S. Andermatt, N. Holmberg, G. K. Schenter, A. Hehn, A. Bussy, F. Belleflamme, G. Tabacchi, A. Glöß, M. Lass, I. Bethune, C. J. Mundy, C. Plessl, M. Watkins, J. VandeVondele, M. Krack and J. Hutter, *J. Chem. Phys.*, 2020, **152**, 194103.
70 G. Lippert, J. Hutter and M. Parrinello, *Mol. Phys.*, 1997, **92**, 477.
71 J. VandeVondele and J. Hutter, *J. Chem. Phys.*, 2007, **127**, 114105.
72 S. Goedecker, M. Teter and J. Hutter, *Phys. Rev. B: Condens. Matter Mater. Phys.*, 1996, **54**, 1703.
73 M. Thomas, M. Brehm, R. Fligg, P. Vöhringer and B. Kirchner, *Phys. Chem. Chem. Phys.*, 2013, **15**, 6608.

